Yitong Zhou

Department of Mechanical and Aerospace Engineering, The Ohio State University, Columbus, OH 43210 e-mail: zhou.1455@osu.edu

Leon M. Headings

Department of Mechanical and Aerospace Engineering, The Ohio State University, Columbus, OH 43210 e-mail: headings.4@osu.edu

Marcelo J. Dapino¹

Professor
Department of Mechanical and Aerospace
Engineering,
The Ohio State University,
Columbus, OH 43210
e-mail: dapino.1@osu.edu

Modeling of Soft Robotic Grippers Integrated With Fluidic Prestressed Composite Actuators

Soft robotic grippers can gently grasp and maneuver objects. However, they are difficult to model and control due to their highly deformable fingers and complex integration with robotic systems. This paper investigates the design requirements as well as the grasping capabilities and performance of a soft gripper system based on fluidic prestressed composite (FPC) fingers. An analytical model is constructed as follows: each finger is modeled using the chained composite model (CCM); strain energy and work done by pressure and loads are computed using polynomials with unknown coefficients; net energy is minimized using the Rayleigh-Ritz method to calculate the deflected equilibrium shapes of the finger as a function of pressure and loads; and coordinate transformation and gripper geometries are combined to analyze the grasping performance. The effects of prestrain, integration angle, and finger overlap on the grasping performance are examined through a parametric study. We also analyze gripping performance for cuboidal and spherical objects and show how the grasping force can be controlled by varying fluidic pressure. The quasi-static responses of fabricated actuators are measured under pressures and loads. It is shown that the actuators' modeled responses agree with the experimental results. This work provides a framework for the theoretical analysis of soft robotic grippers and the methods presented can be extended to model grippers with different types of actuation. [DOI: 10.1115/1.4052699]

Keywords: actuators and transmissions, grasping and fixturing, mechanism design, soft robots

1 Introduction

Soft grippers integrate compliance by replacing rigid structures with soft materials that deform continuously in response to external actuation and interaction with the objects [1]. Such characteristics enable soft grippers to interact more safely with humans, nature, and unstructured environments [2], perform highly dexterous tasks [3], and manipulate delicate objects [4].

Many kinds of mechanisms have been utilized to create soft robots such as a soft gripper with gecko-inspired adhesive [5], a variable stiffness gripper based on layer jamming [6], a soft inflatable module made of elastomer skin [7], and stiffness-tunable robotic links using layer jamming [8,9]. Of the many approaches, those with fluidic elastomer actuators (FEAs) are the most extensively used because of multiple advantages including ease of fabrication, robustness, light weight, and low material cost [10,11]. The actuation of FEAs is obtained by pressurizing a chamber made of highly deformable materials using a fluid (liquid or gas). The structures of FEAs generally have asymmetric geometries or anisotropic materials such that pressurizing the embedded chambers generates expansion in directions that coincide with low stiffness and induces twisting [12], bending [13], and extension or contraction [14].

Various models have been developed for different kinds of FEAs such as finite element and mathematical models for soft FEAs [15], a line-segment model for pleated-type FEAs [16], a thermal dynamics energy model for passive particle jamming actuators [17], and a strain energy model for prestressed composite actuators [18]. These models only analyze single types of actuators, which provides no information in terms of grasping capabilities such as object shape,

size, weight, and requirements on surface condition. Zhou et al. [19] analyzed a soft gripper using a rod-based model. This study is limited to a fixed-sized square object and simple rod-like fingers that inhibit design for more general gripping applications. Yin et al. [20] presented a grasping force model for a soft robotic gripper that is made of shape memory alloys (SMAs) with contraction and stiffness-tunable properties. However, the model only studies the load response of a single finger and no interaction with different shapes of objects is studied.

This paper presents a modeling framework for a soft robotic gripper integrated with multiple fluidic prestressed composite (FPC) actuators. An FPC actuator uses a prestressed elastomeric layer to create the precurved equilibrium shape, and pneumatic pressure is employed to flatten it. A soft gripper composed of precurved actuators takes no effort to hold an object, which makes it energy efficient. In our previous study, a chained composite model (CCM) was proposed for predicting FPC actuator deflections based on inflation pressures and loads [18]. Combining CCM with gripper analysis, this paper provides a set of systematic design rules for creating soft grippers by understanding how grasping performance varies for multiple finger and gripper parameters.

Compared to our previous work and other studies for soft actuators and grippers, the major contributions of this work are as follows. The proposed modeling framework for soft grippers made of FPC actuators allows for direct analysis of grasping performance including grasping force and size. Following a similar procedure, many models for other types of soft actuators [10,11,17,21] can be modified to develop gripper models for analyzing grasping performance. A gripper analysis is presented which defines the parameter design space for soft grippers and identifies the structural relationship between actuators and grippers. This has not been investigated in our previous study [18] or in other studies. The proposed model-based parametric study of grippers provides a design methodology for designers to select structural parameters and pressures to achieve targeted grasping force and size or to predict

¹Corresponding author.

Contributed by the Mechanisms and Robotics Committee of ASME for publication in the JOURNAL OF MECHANISMS AND ROBOTICS. Manuscript received February 17, 2021; final manuscript received October 3, 2021; published online November 15, 2021. Assoc. Editor: K. H. Low.

grasping force and size based on structural parameters and pressures. In addition, lower-order polynomials used in CCM, and this modeling framework enable fast computation, solving in seconds. This modeling framework provides a simple, fast, and practical tool for designing grippers composed of FPC actuators, which can be generalized to other soft grippers.

In this paper, the mechanism of FPC actuators and a soft gripper integrated with FPC actuators are described (Sec. 2). The modeling framework for a soft gripper is developed including CCM for FPC actuators and gripper analysis (Sec. 3). A parametric study is conducted to determine the effects of finger and gripper parameters on grasping capabilities (Sec. 4). A model-based study is carried out for grasping cuboidal and spherical objects (Sec. 5). Finally, the responses of the FPC actuators are measured using a motion capture system and load frame (Sec. 6).

2 Soft Gripper Integrated With Fluidic Prestressed Composite Actuators

2.1 Fluidic Prestressed Composite Actuator Mechanism. A fluidic prestressed composite (FPC) actuator comprises a constraining layer, two elastomeric matrix composite (EMC) layers, and a fluidic layer (Figs. 1(a) and 1(b)). The equilibrium curved shape of the actuator is generated by prestretching the bottom EMC layer before bonding it to the other layers. Pressurizing the actuator flattens it. The concept of such an FPC actuator and an analytical model for small deflections was first presented by Chillara et al. in Ref. [22].

The reinforced elastomers, also known as elastomeric matrix composites (EMC), have unidirectional fibers oriented along the width (90 deg orientation) of the strip. The function of the fibers is to ensure zero in-plane Poisson's ratio. An EMC layer is fabricated by sandwiching two layers of unidirectional carbon fibers between a pair of precured silicone rubber sheets. Prestress is applied to a 90 deg EMC by stretching it along its length before bonding it to the other laminae, hence creating an equilibrium curvature in the FPC actuator. A 90 deg EMC layer without prestress (regular) is included to limit the *Y*-direction expansion upon pressurization.

A fluidic layer is an elastomer layer with embedded fluid channels. To transform pneumatic power into a shape-morphing moment, it is desired to limit the expansion of the fluid channels to only their length (*X* direction) upon pressurization. In the proposed FPC actuator, the expansion in the *Y* direction is constrained by the EMC layers next to it, while in the *Z* direction, the expansion is mitigated by ribs embedded in the fluid channels (details in Sec. 3.1).

A constraining layer is a thin film with a modulus of elasticity much higher than that of the other layers. It is used for constraining the actuator's length and for adding flexural rigidity to the actuator.

The arrangement of laminae in various configurations for composite actuators is investigated in Ref. [22]. The configuration illustrated in Fig. 1(b) is chosen over alternatives for the current study because it produces a larger curvature for the same prestress, leading to a larger grasping stroke when flattened.

2.2 Soft Gripper. A soft gripper is illustrated in Fig. 1(c), where three FPC actuators are clamped by attachments that are fixed to a palm. Upon pressurization, the precurved actuators become flat, which allows the gripper to open. Depressurizing the actuator returns it to its equilibrium precurved shape, thus grasping an object. Depending on the geometrical arrangements of the fingers on the palm, the distance between the free ends of the fingers in their equilibrium state will vary from negative to positive. A negative distance means fingers overlap (Fig. 1(c)) and a positive distance means there is a gap between fingers. The fingers do not actually overlap since they cannot interfere. The formal definition of overlap is described in the following section.

3 Gripper Modeling

In rigid-bodied robots, there are well-defined models to characterize the motion of mechanical linkages and the force they can produce, hence the grasping capability. In this study, a computationally inexpensive analytical model of a soft gripper integrated with FPC actuators is developed to analyze the behavior of both individual actuators and a gripper. The modeling procedure consists of three steps. Step one: transform the input forces from the gripper's coordinate frame to the finger's coordinate frame. Step two: model the finger using the chained composite model (CCM) to determine the output deflected shapes in the finger's coordinate frame based on the input air pressure and the transformed forces. Step three: transform deflections from the finger's coordinate frame to the gripper's coordinate frame to characterize the grasping behavior. Section 3.1 presents the CCM, and Sec. 3.2 describes steps one and three in addition to gripper geometry analysis.

3.1 Chained Composite Model for Fluidic Prestressed Composite Actuators. An FPC actuator is modeled with the chained composite model (CCM) [18], which divides the actuator along its length into multiple elements and models each element based on the assumption of small end slopes. The displacements at

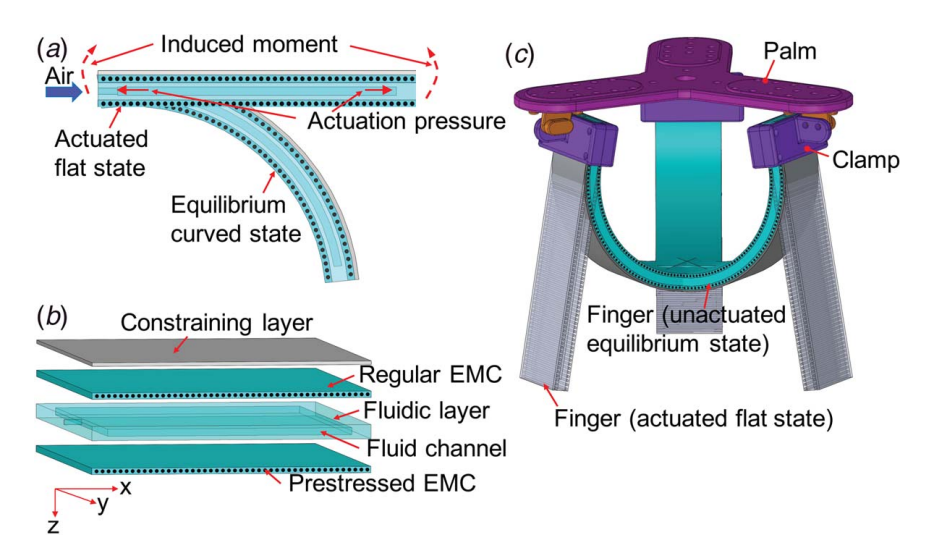


Fig. 1 (a) An FPC actuator in its equilibrium curved and actuated flat shapes, (b) configuration of an FPC actuator, and (c) soft gripper composed of three FPC actuators

points along the length of an element are initially defined based on a polynomial function with unknown coefficients. Cubic polynomials for displacement are sufficient to accurately describe the shape of each element due to small end slopes. The strains along the length of each element are described using a Lagrangian strain formulation in conjunction with classical laminate theory. The tip displacement of the whole actuator is computed using the chain rule. The composite's strain energy and actuation work done by end loads and pressure are then computed using the strains and displacements, and subsequently minimized to obtain a set of nonlinear equations that are a function of the coefficients of the displacement polynomials. These nonlinear equations are solved using the Rayleigh–Ritz method to calculate the shape of each element, which are then combined to determine the shape of the complete composite actuator.

3.1.1 Structures and Geometries. The structure and geometry of the proposed FPC actuator are shown in Fig. 2. Ribs are added to the constraining layer to stiffen the actuator in the Y direction. A longitudinal rib and transverse ribs are embedded in the fluid channel to prevent ballooning in the Z direction upon pressurization, thereby helping to convert the pressure effects into a moment for shape morphing.

The global coordinate frame of an actuator is defined such that the origin of the coordinate is placed L_c from the actuator's end for clamping. Note that the XY plane coincides with the actuator's geometric mid-plane.

3.1.2 Segmentization. An actuator is segmentized along its mid-plane in its deflected equilibrium shape (Fig. 3(a)), where the actuator is subject to a prestrain of ϵ_0 , tip load components F_z and F_x , and pressure P_f . The original length of the actuator's main part that is used for grasping objects is L_x , which corresponds to the state where no deflections or prestresses are applied. The

actuator is segmented into N elements and the local coordinate frame for the first element $(X_1O_1Z_1)$ corresponds to the global coordinate frame (XOZ). The local coordinate frame of the ith element $(X_iO_iZ_i,\ 2\leq i\leq N)$ is attached to and moves along with the free end of the (i-1)th element, i.e., O_i (Fig. 3(b)). The length of each element without prestress or deflection (straight) is denoted by L_i , where $\sum_{i=1}^N L_i = L_x$. The end slope for the ith element is defined as η_i and the angle between OX_i and OX as θ_i . Small end slopes require $\partial w_0/\partial x < 1$ per Ref. [23], where w_0 is the Z-direction displacement. This relationship results in approximately $\eta_i < 45$ deg. For instance, to model an approximately quarter-circle shaped composite as shown in Fig. 3(a), at least two elements would be required. However, higher model accuracy requires more elements.

3.1.3 Strain Energy of the ith Element. A mechanically prestressed composite actuator is modeled based on the assumptions of classical laminate plate theory. The in-plane strains of an arbitrary point in the *i*th element of the actuator, defined using a Lagrangian description per von Karman's hypothesis [24], are expressed in relation to that point's displacements (u_i, v_i, w_i) in the X_i , Y_i , and Z_i directions (local coordinate frame) as

$$\epsilon_{ix} = \frac{\partial u_i}{\partial x} + \frac{1}{2} \left(\frac{\partial w_i}{\partial x} \right)^2$$

$$\epsilon_{iy} = \frac{\partial v_i}{\partial y} + \frac{1}{2} \left(\frac{\partial w_i}{\partial y} \right)^2$$

$$\gamma_{ixy} = \frac{\partial u_i}{\partial y} + \frac{\partial v_i}{\partial x} + \frac{\partial w_i}{\partial x} \frac{\partial w_i}{\partial y}$$
(1)

The out-of-plane strains are zero as a result of the Kirchhoff hypothesis, which is used to determine the displacement field in classical

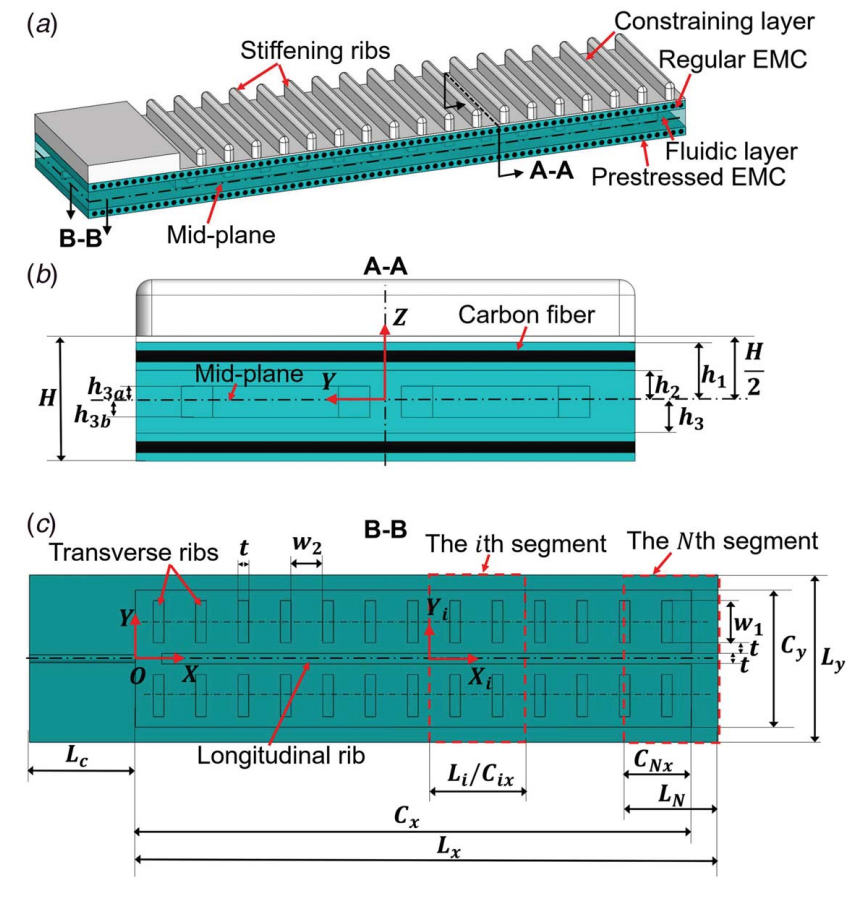


Fig. 2 (a) Geometry of an FPC actuator, (b) section view A-A, and (c) section view

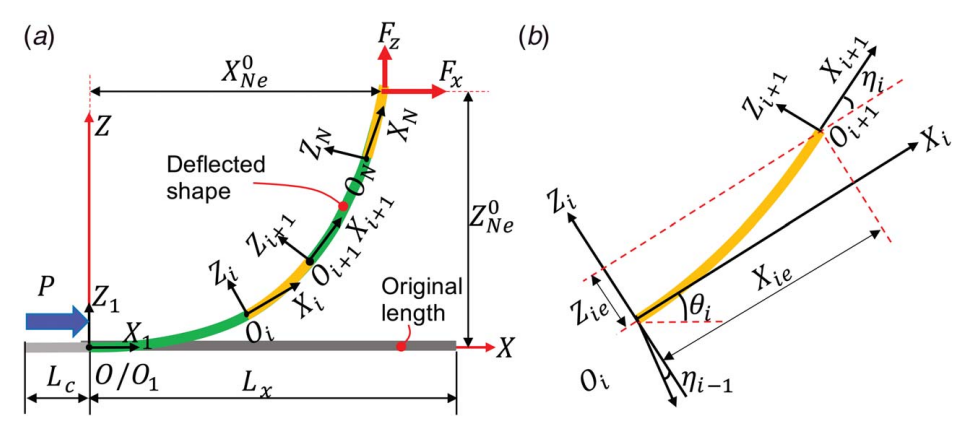


Fig. 3 (a) Segmentization of an actuator along its mid-plane in its deflected equilibrium state and (b) the *i*th element in its deflected equilibrium state

plate theory [24]. Using subscripts i and 0 to denote the ith element and mid-plane, respectively, displacements (u_i, v_i, w_i) are related to the displacements of the geometric mid-plane in the local coordinates (u_{i0}, v_{i0}, w_{i0}) as

$$u_{i} = u_{i0} - z \frac{\partial w_{i0}}{\partial x}$$

$$v_{i} = v_{i0} - z \frac{\partial w_{i0}}{\partial y}$$

$$w_{i} = w_{i0}$$
(2)

Strains of an arbitrary plane z for the ith element are obtained by substituting Eq. (2) into Eq. (1) as

$$\epsilon_{ix} = \frac{\partial u_{i0}}{\partial x} + \frac{1}{2} \left(\frac{\partial w_{i0}}{\partial x} \right)^2 - z \left(\frac{\partial^2 w_{i0}}{\partial^2 x} \right)$$

$$\epsilon_{iy} = \frac{\partial v_{i0}}{\partial y} + \frac{1}{2} \left(\frac{\partial w_{i0}}{\partial y} \right)^2 - z \left(\frac{\partial^2 w_{i0}}{\partial^2 y} \right)$$

$$\gamma_{ixy} = \frac{\partial u_{i0}}{\partial y} + \frac{\partial v_{i0}}{\partial x} + \frac{\partial w_{i0}}{\partial x} \frac{\partial w_{i0}}{\partial y} - 2z \left(\frac{\partial^2 w_{i0}}{\partial x \partial y} \right)$$
(3)

The displacements along the geometric mid-plane for the ith element in the X_i , Y_i , and Z_i directions are described using polynomials as

$$u_{i0} = a_{i1}x + a_{i3}x^3, \quad w_{i0} = c_{i2}x^2, \quad v_{i0} = b_{i1}y$$

$$(0 \le x \le L_i, \quad -L_v/2 \le y \le L_v/2, \quad i \in [1, \dots, N])$$
(4)

Substituting Eq. (4) into Eq. (3), strains of an arbitrary plane z of the actuator are computed as

$$\epsilon_{ix} = 2c_{i2}^2x^2 - 2zc_{i2} + 3a_{i3}x^2 + a_{i1}$$
 $\epsilon_{iy} = b_{i1}$
 $\gamma_{ixy} = 0$
(5)

The strain energy $\Psi_{(i)}$ for the *i*th element of the actuator is expressed in terms of the laminae's geometries, strains, and plane-stress-reduced stiffnesses Q_{pq} [24] as

$$\Psi_{(i)} = \int_{V_i} \left(\frac{1}{2} Q_{11} \epsilon_{ix}^2 + Q_{12} \epsilon_{ix} \epsilon_{iy} + \frac{1}{2} Q_{22} \epsilon_{iy}^2 + \frac{1}{2} Q_{16} \gamma_{ixy} \epsilon_{ix} \right. \\
\left. + \frac{1}{2} Q_{26} \gamma_{ixy} \epsilon_{iy} + \frac{1}{2} Q_{66} \gamma_{ixy}^2 \right) dV_i \tag{6}$$

where V_i is the material volume of the *i*th element and Q is a function of Poisson's ratio ν and elastic modulus E. Since it is observed that $\gamma_{ixv} = 0$ in Eq. (5), $\Psi_{(i)}$ is further written as

$$\Psi_{(i)} = \int_{V_i} (\Psi_{11} + \Psi_{12} + \Psi_{22}) \, \mathrm{d}V_i \tag{7}$$

where Ψ_{11} , Ψ_{12} , and Ψ_{22} denote $0.5Q_{11}\epsilon_{ix}^2$, $Q_{12}\epsilon_{ix}\epsilon_{iy}$, and $0.5Q_{22}\epsilon_{iy}^2$, respectively. The material properties are different for each lamina, hence their strain energies are written separately. For example, Ψ_{11} for the constraining layer is $\Psi_{11}^{(FL)} = 0.5Q_{11}^{(CL)}\epsilon_{ix}^2$. The limits of integration for different layers in the *i*th element are shown in Table 1.

We assume the constraining layer thickness to be constant since the stiffening ribs in this lamina retain no strain energy other than the negligible amount near the root of the ribs. The length of the fluid channel in the *i*th element C_{ix} equals L_i for all elements but the *N*th due to the wall of the fluidic layer (Fig. 2(c)).

The strain energy of the *i*th element's prestressed EMC layer is computed in a semi-empirical form as

$$\Psi_{PEMC(i)} = \int_{0}^{L_{i}} \int_{-Ly/2}^{Ly/2} \int_{-H/2}^{-h_{3}} \left(\frac{-0.698 \times 10^{6}}{5} (\epsilon_{0} - \epsilon_{ix})^{5} + \frac{2.29 \times 10^{6}}{4} (\epsilon_{0} - \epsilon_{ix})^{4} + \frac{-2.306 \times 10^{6}}{3} (\epsilon_{0} - \epsilon_{ix})^{3} + \frac{1.598 \times 10^{6}}{2} (\epsilon_{0} - \epsilon_{ix})^{2} + \Psi_{22}^{(EMC)} \right) dz dy dx$$
(8)

where ϵ_0 is the prestrain applied and the coefficients are derived experimentally from a uniaxial tensile test [22]. It is noted that the $\Psi_{12}^{(EMC)}$ term disappears in Eq. (8) since $Q_{12}^{(EMC)} = 0$ when the Poisson's ratio for the EMC layer is zero.

The strain energy of the *i*th element's fluidic layer is computed by subtracting the strain energy of the void volume from the whole volume, which is written as

$$\Psi_{FL(i)} = \Psi_{whole(i)} - \Psi_{channel(i)} + \Psi_{ribs(i)} \tag{9}$$

Table 1 Limits of integration for the computation of the potential energy for the *i*th element of an FPC actuator

Lamina	z	У	х	
Constraining layer	$(h_1, 0.5H)$	$(-0.5L_y, 0.5L_y)$	$(0, L_i)$	
Regular EMC Prestressed EMC	(h_2, h_1) $(-0.5H, -h_3)$	$(-0.5L_y, 0.5L_y)$ $(-0.5L_y, 0.5L_y)$	$(0, L_i)$ $(0, L_i)$	
Fluidic layer (whole)	$(-h_3, h_2)$	$(-0.5L_y, 0.5L_y)$	$(0, L_i)$	
Fluidic layer (channel)	$(-h_{3b},h_{3a})$	$(-0.5C_y, 0.5C_y)$	$(0, C_{ix})$	

where $\Psi_{whole(i)}$ and $\Psi_{channel(i)}$ are the strain energies calculated with the fluidic layer's whole volume and the channel volume without ribs using the limits in Table 1. The strain energy of the ribs inside the fluid channel for the *i*th element $\Psi_{ribs(i)}$ can be computed based on the coordinates of the ribs in the element's local coordinate frame [18].

3.1.4 Chain Rule and Work Done by Loads. To obtain the work done by loads, a chain rule based on coordinate transformation is used to calculate the tip displacement of the Nth element in the global coordinate frame (OXZ). The deflected equilibrium position of the ith element's mid-plane in the local coordinate frame ($X_iO_iZ_i$) is computed based on the displacements in Eq. (4) as

$$X_{i0} = x + u_{i0} = (a_{i1} + 1)x + a_{i3}x^{3}$$

$$Z_{i0} = w_{i0} = c_{i2}x^{2}$$
(10)

Using subscript ie to denote the end of the ith element, then, the deflected position of the end of the ith element's mid-plane in $X_iO_iZ_i$ is

$$X_{ie} = (a_{i1} + 1)L_i + a_{i3}L_i^3$$

$$Z_{ie} = c_{i2}L_i^2$$
(11)

Using superscript 0 to represent the actuator's global coordinate frame, the deflected position of the end of the ith element's midplane in OXZ is computed as

$$\begin{bmatrix} X_{ie}^0 \\ Z_{ie}^0 \end{bmatrix} = \begin{bmatrix} 1 & 0 & \cos\theta_i & -\sin\theta_i \\ 0 & 1 & \sin\theta_i & \cos\theta_i \end{bmatrix} \begin{bmatrix} X_{(i-1)e}^0 \\ Z_{(i-1)e}^0 \\ X_{ie} \\ Z_{ie} \end{bmatrix}$$
(12)

where θ_i and η_i are calculated as

$$\theta_{i} = \sum_{k=1}^{i-1} \eta_{k} \ (i \in [2, ..., N]), \ \theta_{1} = 0$$

$$\eta_{i} = \arctan\left(\frac{\partial Z_{i0}/\partial x}{\partial X_{i0}/\partial x}\right)\Big|_{(x=L_{i})}$$

$$= \arctan\left(\frac{2c_{i2}L_{i}}{(a_{i1}+1)L_{i}+3a_{i3}L_{i}^{2}}\right)$$
(13)

By recursively calling Eqs. (12) and (13), the deflected position of the end of the *N*th element's mid-plane in *OXZ* of the actuator (X_{Ne}^0, Z_{Ne}^0) , which equals the deflected end position of the actuator's mid-plane in *OXZ*, is expressed with polynomial coefficients $K_i = \{a_{i1}, a_{i3}, b_{i1}, c_{i2}\}$ and L_i for all elements. Therefore, the displacement of the end of the *N*th element's mid-plane in *OXZ* is computed as

$$u_{Ne}^{0} = X_{Ne}^{0} - L_{x}, w_{Ne}^{0} = Z_{Ne}^{0}$$
(14)

Then, variational work done by F_x and F_z on the actuator is expressed as

$$\delta W_F = F_x \delta u_{Ne}^0 + F_z \delta w_{Ne}^0 \tag{15}$$

3.1.5 Work Done by Pressure. The work done on the composite's ith element by the pneumatic source is expressed as

$$W_{P(i)} = \frac{-PV_{(i)}}{\gamma - 1} = \frac{-P\int_{V_i} (1 + \epsilon_{ix})(1 + \epsilon_{iy})dV_i}{\gamma - 1}$$
(16)

where $\gamma = 1.4$ is the adiabatic index, P is the actuation pressure, and $V_{(i)}$ is the actuated volume of the ith segment's fluid channel, which is the same as the volume in $\Psi_{channel(i)} - \Psi_{ribs(i)}$ and can be integrated in the same way.

3.1.6 Computation of Actuator Shape. The net energy is computed and minimized using the variational Rayleigh–Ritz method to calculate the equilibrium deflected shape of the actuator as a function of the actuation pressure and end loads:

$$\frac{\partial (\sum_{1}^{N} \Psi_{(i)}) - \partial (\sum_{1}^{N} W_{P(i)}) - \partial W_{F}}{\partial K_{i}} = 0, \quad i \in [1, \dots, N]$$
 (17)

where $K_i = \{a_{i1}, a_{i3}, b_{i1}, c_{i2}\}$. The expressions for $\Psi_{(i)}$, $W_{P(i)}$, W_F , and their partial derivatives are derived in symbolic form using MATLAB. The Rayleigh–Ritz method is a classical variational method that is in the form of a finite linear combination of undetermined parameters and chosen functions. A detailed explanation of this method is given in Ref. [24]. The 4N nonlinear equations resulting from Eq. (17) are then solved numerically in MATLAB using the Newton–Raphson approach.

3.2 Gripper Analysis. The gripper design can be tuned by varying a number of parameters including the number of fingers, the angle between each pair of adjacent fingers, finger mounting angle α , palm size l, clamp length L_c , finger full-length L, and finger prestrain ϵ_0 (Fig. 4). Changing any of these parameters will result in different grasping performance.

For demonstration purposes, a four-finger, single-palm setup is shown in Fig. 4(a). The angle between each pair of adjacent fingers is 90 deg. Note that this analysis is not limited to four fingers but can be generalized to other numbers of fingers as long as the fingers are distributed along the same circle on the palm and the assumptions made below are satisfied.

In order to make the theoretical model more tractable for analysis, we only examine gripping mechanisms that involve point contact with an object. In addition, we assume that every finger bends in a plane and the curvature does not reverse the sign, which means fingers cannot twist or bend backward. Since the fingers are usually much thinner than the objects, we also assume that the fingers have zero thickness in the gripper analysis. Therefore, the actuator's mid-plane is used to represent the finger. Figure 4(b)illustrates grasping with different sized objects where two fingers located at opposite sides of the palm are shown. The soft gripper is pointing downwards. We let d denote the grasping size at the grasping location. Figures 4(c) and 4(d) show nonsymmetrical and symmetrical grasping, where the normal force F and friction force f are exerted on the object perpendicular and tangential to the contact surface, respectively. For simplicity, we assume all fingers share the same force and curvature and are synchronized (Fig. 4(d)). Thus, by symmetry, it is sufficient to analyze a single finger as shown in Fig. 4(e), where the coordinate frames for the finger and the gripper are defined as XOZ and $X_gO_gZ_g$, respectively. Note that XOZ coincides with the finger's global coordinate frame in Sec. 3.1. The grasping angle β is defined as the angle between F and the X_g axis. We let l_0 denote the projection of the finger on the positive X_g axis. The notation used for the gripper analysis is listed in Table 2.

3.2.1 Parameter Design Space. In order to obtain the relationship between the gripper parameters and grasping performance, we first constrain the design space for the design parameters α and l based on three requirements: the minimum size the gripper can grasp is zero, the maximum size the gripper can grasp is always greater than or equal to palm size l, and the minimum weight the gripper can grasp is always greater than or equal to zero, i.e.,

$$d_{\min} = 0, \quad d_{\max} \ge l, \quad G \ge 0$$
 (18)

The first requirement allows no gap between the fingers in their equilibrium precurved states, hence preventing objects from slipping through a gap between the fingers. The second requirement enables a relatively large maximum grasping size. The third requirement ensures that the gripper can lift some weight for all of the fingers' viable shapes.

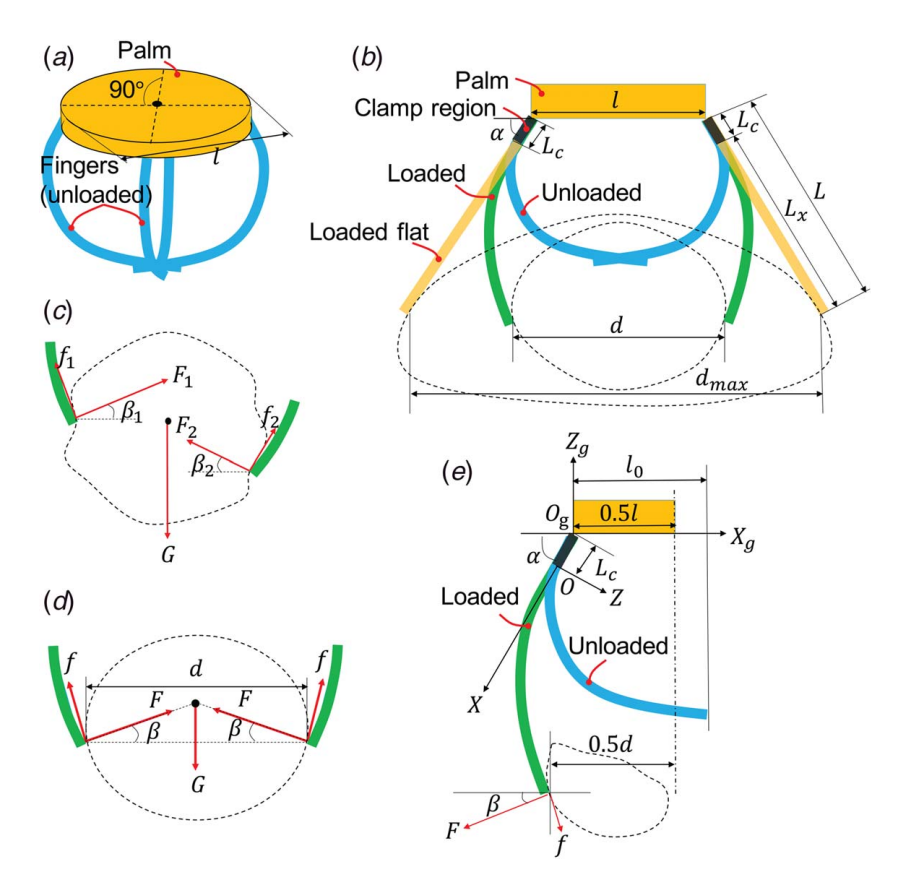


Fig. 4 (a) Schematic representation of a four-finger gripper, (b) grasping demonstration, (c) nonsymmetrical grasping, (d) symmetrical grasping, and (e) single finger geometry based on symmetry

Table 2 Notation for gripper analysis

Notation	Definition			
F	Normal force applied to the finger			
f	Friction force applied to the finger			
d	Grasping size			
g	Overlap between fingers			
\tilde{L}	Finger full length			
L_c	Clamp length			
1	Palm size			
l_0	Projection of the finger on positive X_g Prestrain applied to the finger Mounting angle Grasping angle			
ϵ_0				
α				
β				
Δ_{rg}	Finger tip displacement on X_g			
$\Delta_{\tau g}^{\gamma_0}$	Finger tip displacement on Z_g^s			
XÕZ	Finger's coordinate frame			
$X_g O_g Z_g$	Gripper's coordinate frame			

When the fingers are in the equilibrium precurved state, d achieves the minimum, which is expressed as

$$d_{\min} = \max(0, l - 2l_0) \tag{19}$$

Since no gap between the fingers is allowed in their equilibrium precurved states, i.e., $d_{\min} = 0$, palm size l is constrained to $l \le 2l_0$, where l_0 depends on mounting angle α , prestrain ϵ_0 , and finger length L. The overlap between fingers is defined formally as

$$g = l_0 - 0.5l \tag{20}$$

which is greater than or equal to 0 since $l \le 2l_0$.

When the fingers are loaded to be fully flat (Fig. 4(b)), d achieves the maximum value, which is computed as

$$d_{\max} = l + 2L\cos\alpha \tag{21}$$

It is observed that d_{\max} increases with palm size l and finger length L and decreases with increasing α . When actuated to be flat, it is found that $\alpha = \beta$; hence, the force balance on the object is

$$4f \sin \alpha = 4F \cos \alpha + G \le 4\mu F \sin \alpha \tag{22}$$

where μ is the static coefficient of friction between the finger and the object. Reexpressing Eq. (22) as $G \le 4F(\mu \sin \alpha - \cos \alpha)$, it is obtained that $\mu \sin \alpha - \cos \alpha \ge 0$ due to the constraint of $G \ge 0$. In this paper, the elastomer used in the actuator is rubber. For clean and dry rubber, the static coefficient of friction between rubber and other materials is normally within the range [0.25, 0.85]. Choosing $\mu = 0.6$, α is constrained to $\alpha \ge \operatorname{arccot}\mu \approx \pi/3$. When $\alpha > \pi/2$, it is obtained that $d_{\max} < l$, which means the grasping size is less than the palm size, and the grasping capability is impaired. Hence, α is further constrained to $\alpha \le \pi/2$. Therefore, the mounting angle α is required to be within $[\pi/3, \pi/2]$. However, for a contact surface with a higher friction coefficient, the lower limit for the mounting angle α can be further reduced, which results in a larger d_{\max} , i.e., a larger maximum grasping size.

The constraints derived for mounting angle α and palm size l are listed as

$$\alpha \in [\pi/3, \pi/2], \ l \le 2l_0$$
 (23)

3.2.2 Coordinate Transformation Between Gripper and Finger. Since deflections of the finger are modeled in the finger's coordinate frame XOZ using CCM, the transformation of forces and deflections between the two coordinate frames is carried out

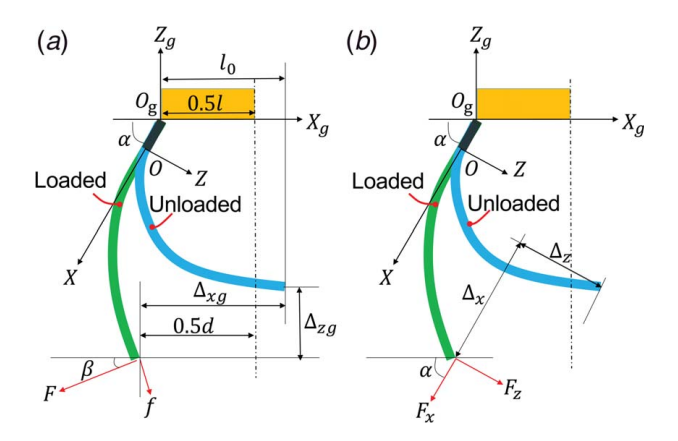


Fig. 5 (a) Displacements in the gripper's coordinate frame and forces applied to one finger by the object and (b) displacements and forces in one finger's coordinate frame

to analyze the behavior of the gripper in the gripper's coordinate frame $X_g O_g Z_g$. Figure 5(a) shows the displacements of the finger in the gripper's coordinate frame and the forces applied to the finger by the object based on the object's shape. Figure 5(b) shows the displacements and forces in the finger's coordinate frame.

The forces in the finger's coordinate frame (XOZ) are expressed

$$\begin{bmatrix} F_x \\ F_z \end{bmatrix} = \begin{bmatrix} \cos(\alpha - \beta) & \sin(\alpha - \beta) \\ -\sin(\alpha - \beta) & \cos(\alpha - \beta) \end{bmatrix} \begin{bmatrix} F \\ f \end{bmatrix}$$
 (24)

Inputting zero end load and zero pressure to the CCM, one can obtain the unloaded equilibrium deflected shape of the finger (Fig. 5). Then, zero pressure and the transformed end loads F_x and F_z are input to the CCM to obtain the loaded equilibrium deflected shape, from which displacements Δ_x and Δ_z in the finger's coordinate frame can be calculated. Displacements in the gripper's coordinate frame $(X_g O_g Z_g)$ are then calculated as

$$\begin{bmatrix} \Delta_{xg} \\ \Delta_{zg} \end{bmatrix} = \begin{bmatrix} \cos \alpha & \sin \alpha \\ \sin \alpha & -\cos \alpha \end{bmatrix} \begin{bmatrix} \Delta_x \\ \Delta_z \end{bmatrix}$$
 (25)

3.2.3 Grasping Behavior. Grasping size and grasping weight are the key grasping performance metrics for a soft gripper. Based on the geometrical relationship and calculated deflections, the grasping size is expressed as

$$d = 2(\Delta_{xg} - g) = 2(\Delta_{xg} + 0.5l - l_0)$$
 (26)

In addition, the vertical lifting force a finger can provide is calculated as

$$f_{v} = f \cos \beta + F \sin \beta \tag{27}$$

4 Model-Based Parametric Study of Gripper

In order to enable design optimization for a soft gripper integrated with FPC actuators, parametric studies are conducted to develop a thorough understanding of how different design parameters affect grasping performance including grasping size and vertical lifting force. The influences of design parameters including prestrain, mounting angle, and fingers' overlap on gripper response are examined through a parametric study. All parametric studies are conducted with CCM using eight segments, which was found to be sufficient to represent the actuator response in our previous study [18]. The pressure is set to be zero, and only forces are input to CCM in this study. Note that in this paper, the values of L_x and L_c are maintained at 110 mm and 20 mm, respectively. In addition, β is maintained at 0 throughout this section, so that F is horizontal, f is vertical, and $f_y = f$. In order to characterize the maximum grasping

Table 3 Dimensions of a single FPC actuator used for modeling and fabrication (units: mm)

L_x	L_{y}	L_c	C_x	C_y	Н	h_1	h_2	h_3	h_{3a}
110	31.75	20	105	26	8.2	3.7	1.8	2.2	0.8
h_{3b}	w_1	w_2	t						
1.2	8.0	6.0	2.0						

Table 4 Material properties and thicknesses of the laminae used for modeling and fabrication

	Thickness (mm)	E ₁ (MPa)	E ₂ (MPa)	$\nu_1 = \nu_2$
Constraining layer (PP)	0.4	305	305	0.43
Fluidic layer (silicone rubber)	4.0	1.2	1.2	0.48
Regular EMC (fiber reinforced rubber)	1.9	1.5	250	0
Prestressed EMC	1.9	Nonlinear	250	0

capabilities, f is set to be μF , where $\mu = 0.6$. Here, μ was set to be 0.6 as an example. One may choose a different value for μ depending on the friction coefficient between the gripper and the object being grasped. Hence, f is the maximum vertical lifting force the finger can provide. The FPC actuator structure (Fig. 2) is employed with the dimensions and the material properties shown in Tables 3 and 4.

The computational time for computing the shape of a finger for each case in this section took less than 5 s using a MacBook (early 2015 model).

4.1 Parametric Study of Prestrain and Mounting Angle.

For a given set of construction materials, prestrain and mounting angle have a major influence on the gripper's grasping performance including grasping size and vertical lifting force. In this work, we set $l=2l_0$, which means there is no overlap between fingers in their equilibrium precurved states. Three prestrains, 0.4, 0.25, and 0.15, are modeled with three mounting angles $\pi/2$, $\pi/2.5$, and $\pi/3$.

The responses of the mid-plane of a composite finger varying with F and $f = \mu F$ for different prestrains with mounting angles $\pi l / 2$ and $\pi l / 3$ are plotted in Fig. 6. It is observed that higher prestrains generate larger curvatures and increasing end loads flattens the finger. The projection of the finger on the positive X_g axis is 0.5l due to $l = 2l_0$ and is found to increase with mounting angle.

The maximum vertical lifting force versus grasping size results are illustrated in Fig. 7(a) for different prestrains and mounting angles. It is observed that the larger the prestrain, the higher the lifting force the finger provides. In addition, actuators with larger mounting angles provide higher forces than smaller angles, and the difference decreases with prestrain. It is noted that the curve with $\epsilon_0 = 0.4$, $\alpha = \pi/2$ has a kink. This is because the projection of the finger on the positive X_g axis l_0 is greater than l/2 (see the plot with $\epsilon_0 = 0.4$, $\alpha = \pi/2$ in Fig. 6). All curves start from zero due to the constraint of zero overlap between fingers, $l=2l_0$, which allows the fingers to contact each other without force in their equilibrium precurved state. In summary, larger prestrains enable grasping larger and heavier objects. However, when grasping smaller objects, the outsides of the fingers are facing the objects, which is not desired for grasping. Smaller prestrains are preferred for grasping smaller and lighter objects.

Figure 7(b) shows the relationship between maximum grasping size d_{max} and mounting angle α , where d_{max} is expressed in Eq. (21). In general, higher prestrains and smaller mounting angles result in larger d_{max} . In addition, d_{max} decreases with increasing mounting angle for larger prestrains and shows a different trend for the smallest prestrain. This is because the effect of the prestrain

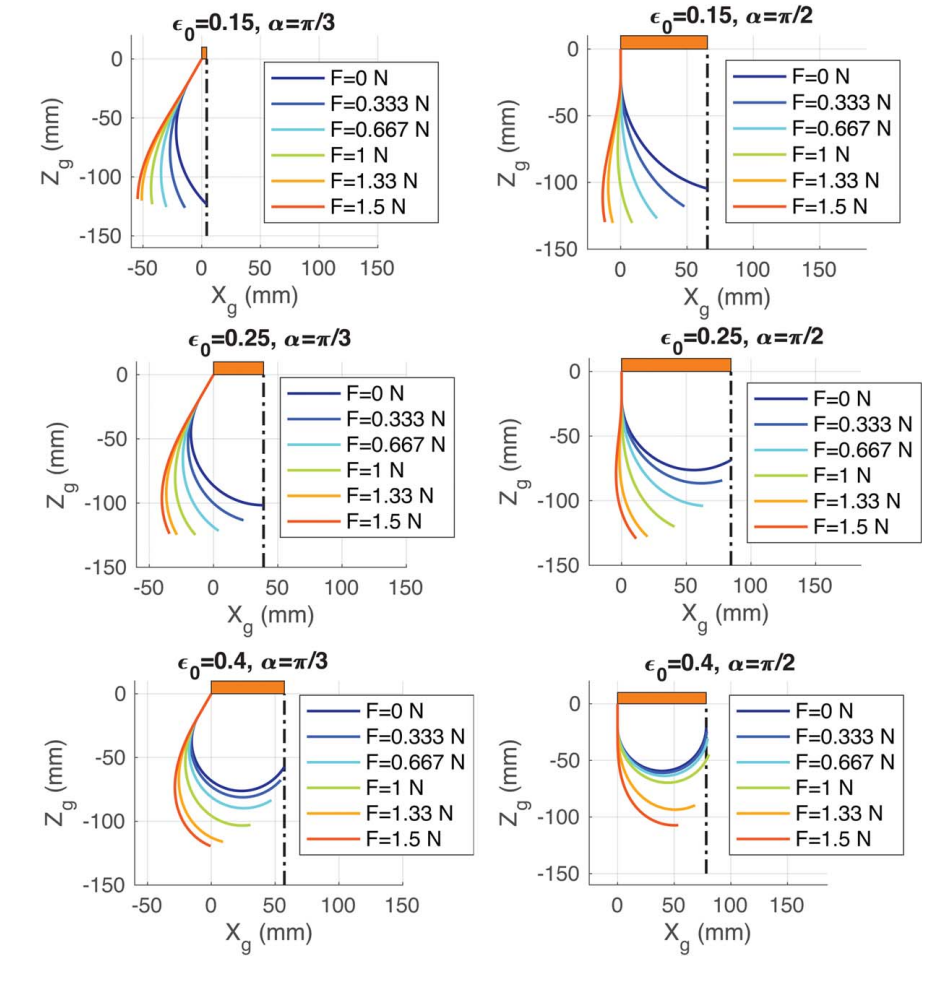


Fig. 6 Modeled shapes of initially curved composite actuators for different prestrains and mounting angles in the gripper

on $d_{\rm max}$ is highly dependent on the constraint provided by $l=2l_0$, where l_0 increases with prestrain and mounting angle. If we fix l and drop the constraint $l=2l_0$, $d_{\rm max}$ will only depend on α and decrease with increasing α based on Eq. (21).

4.2 Parametric Study of Finger Overlap. In Sec. 4.1, it is found that the gripper provides zero vertical lifting force for a zero-sized object due to the constraint of zero overlap between fingers in their unloaded equilibrium state. However, it is desired to design a gripper that is also capable of lifting extremely small objects. Such capability can be provided by introducing an overlap between fingers in their equilibrium state. To study the effects of the finger overlap on grasping performance, the CCM is run with a prestrain of 0.25 for different values of mounting angle and overlap.

The maximum vertical lifting force versus grasping size results are illustrated in Fig. 8(a) for all overlaps and mounting angles. Again, it is observed that the larger the mounting angle, the larger the maximum lifting force. In addition, increasing overlap g increases lifting force for a given grasping size d. In general, introducing overlap between fingers is equivalent to shifting μF versus d curves to the left by the amount of overlap, hence providing a nonzero lifting force for even extremely small objects.

Figure 8(b) shows the relationship between d_{max} and g for different α , where d_{max} can be rewritten as

$$d_{\text{max}} = 2(l_0 - g + L\cos\alpha) \tag{28}$$

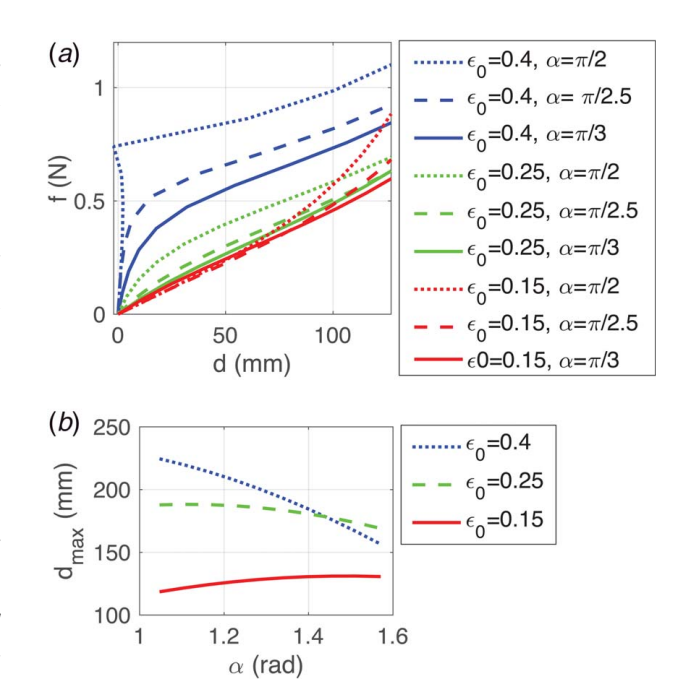


Fig. 7 Parametric analysis results for different actuator prestrains and mounting angles: (a) maximum vertical lifting force versus gripper grasping size and (b) maximum grasping size versus mounting angle

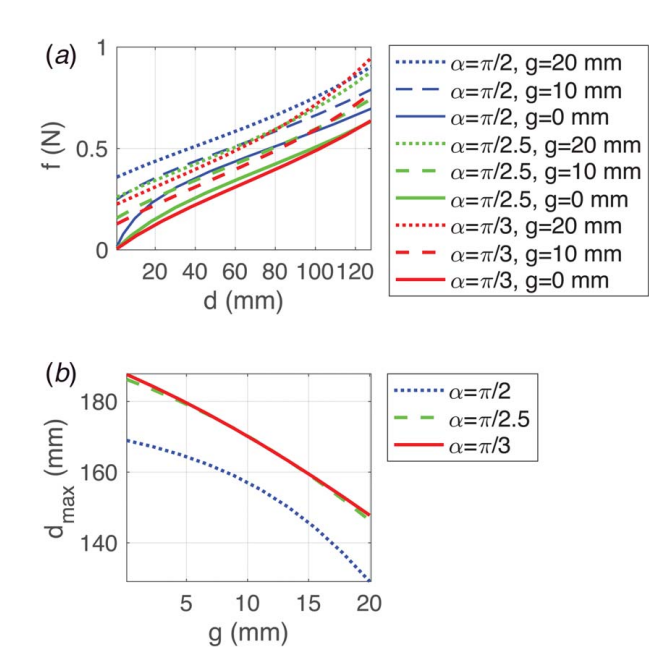


Fig. 8 Parametric analysis results for different overlaps with a prestrain of 0.25: (a) maximum vertical lifting force versus grasping size and (b) maximum gripper grasping size versus finger overlap

It is observed that grippers with fingers at mounting angles $\pi/2.5$ and $\pi/3$ have similar maximum grasping sizes. This is because grippers with fingers at $\alpha = \pi/2.5$ have larger l_0 and mounting angles than fingers with $\alpha = \pi/3$, which results in similar $d_{\rm max}$, as indicated in Eq. (28). In addition, grippers with fingers at $\alpha = \pi/2$ have smaller maximum grasping sizes than at the other two mounting angles for all overlaps.

5 Model-Based Study of Grasping Cuboidal and Spherical Objects

In order to characterize the grasping capabilities of a soft gripper with FPC actuators, case studies are conducted with objects of two common shapes: cuboid and sphere. The grasping capabilities investigated include grasping size and vertical lifting force. For grasping fragile objects, the grasping contact force is a key factor for a successful grasp. Hence, a model-based analysis of grasping contact force is conducted by varying the input pressure for a cuboidal object. In this study, the values of prestrain, mounting angle, and overlap between fingers are maintained at 0.25, $\pi/3$, and 20 mm, respectively. These values are selected because they provide large maximum lifting force and maximum grasping size as shown in Sec. 4. Geometry, dimensions, and material properties of the actuator are the same as those shown in Fig. 2, Table 3, and Table 4, respectively.

5.1 Grasping Cuboidal Objects

5.1.1 Grasping Capability. The grasping of a cuboid object is illustrated in Fig. 9(a), where it is noted that β is zero (flat contact surface parallel to the Z_g axis). In order to characterize the maximum grasping capabilities, f is set to be μF . Then, the maximum vertical lifting force versus grasping size d is plotted in Fig. 9(b). This study is equivalent to the study in Sec. 4.2 with $\alpha = \pi/3$ and g = 20 mm due to the same parameter setup. Hence, the maximum vertical lifting force curve in Fig. 9(b) equals the curve with $\alpha = \pi/3$ and g = 20 mm in Fig. 8(a). The area on and under the curve is the grasping region, which represents the range of object size d and weight per finger f for which a cuboidal object can be grasped. For example, a cuboid with d = 100 mm and 0.3 N per finger can be grasped.

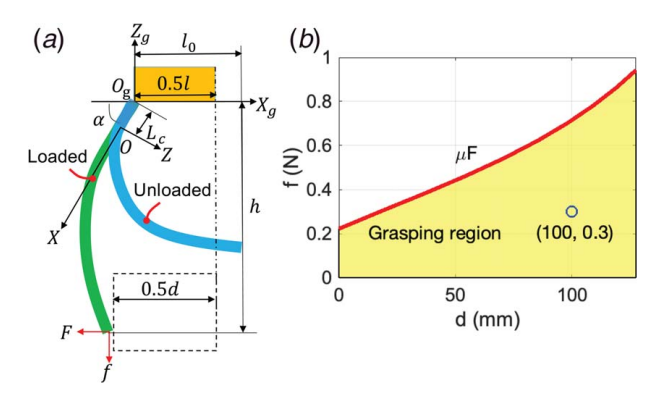


Fig. 9 Grasping capability for cuboidal objects: (a) displacements and forces for one gripper finger and (b) grasping region, representing the range of object size and weight per finger that can be grasped

5.1.2 Force Control by Varying Pressure. In order to control the grasping contact force applied to a fragile object while maintaining firm grasping, it is desired to know the grasping state of the fingers, including forces and shapes. However, the CCM takes input forces and pressure and outputs deflections of each finger, from which one cannot obtain forces by inputting deflections directly. Hence, we propose an indirect method that consists of three steps to find F, f, and finger shape. We choose a cuboid with d = 100 mm and f = 0.3 N per finger as an example, which was found to be in the grasping region. Step one: run the CCM with a desired pressure using different combinations of F and f, where $f \le \mu F$; find out d; and plot F, f, and the CCM-modeled d as a F - f - d surface. Step two: find F at the intersection of three surfaces including the F-f-d surface, and surfaces of d=100 mm and f = 0.3 N (Fig. 10(a)). Step three: input F and f to the CCM to find finger shape. To find F at different pressures, F-f-d surfaces for different pressures are computed and the intersections are found with the three steps above as illustrated in Fig. 10(b). It is observed that the F - f - d surfaces for different pressures are almost parallel to each other. The modeled shapes of a finger with the calculated F, f = 0.3 N, and pressure are shown in Fig. 10(c), where it is observed that the fingers have similar shapes although the curvature decreases slightly with increasing pressure. We define h as the height of each finger along the Z_g axis (Fig. 9(a)). It is found that the higher the pressure, the lower the grasping contact force F, and the slightly lower the finger height h (Fig. 10(d)). The F versus pressure curve is almost linear, with which an open-loop control of grasping contact force can be conveniently developed.

5.2 Grasping Spherical Objects

5.2.1 Grasping Capability. Grasping a sphere is more complex than grasping a cuboid since the grasping angle β varies with grasping location. We define positive β as grasping a sphere on its lower half and negative β as grasping on the upper half, as shown in Figs. 11(b) and 11(c), respectively. As β becomes more negative, one expects the lifting force to become smaller, hence failing to grasp the object. From Eq. (27), it is further derived that $f_{\nu} \leq F(\mu \cos \beta + \sin \beta)$. In order to have $f_{\nu} \geq 0$, we require $\mu \cos \beta + \sin \beta \geq 0$ or $\tan \beta \geq -\mu = -0.6$. Hence, β is constrained to $-\pi/6 \leq \beta \leq \pi/2$.

The maximum grasping radius can be obtained from $2r_{\rm max}\cos\alpha = d_{\rm max} = l + 2L\cos\alpha$ to be $r_{\rm max} = (l/2 + L\cos\alpha)/\cos(-\pi/2 + \alpha)$.

To determine the maximum vertical lifting force, f is set equal to μF with μ equal to 0.6, hence $f_{\nu} = F(\mu \cos \beta + \sin \beta)$. The pressure is maintained at zero. Then, the CCM is run by varying F for different β . Figures 12(α) and 12(α) show the modeled shapes of fingers at $\beta = 0.852$ rad and $\beta = -0.284$ rad, respectively. Note that the finger is not open for low force so that opposing fingers still overlap with each other, in which case no spheres can be grasped

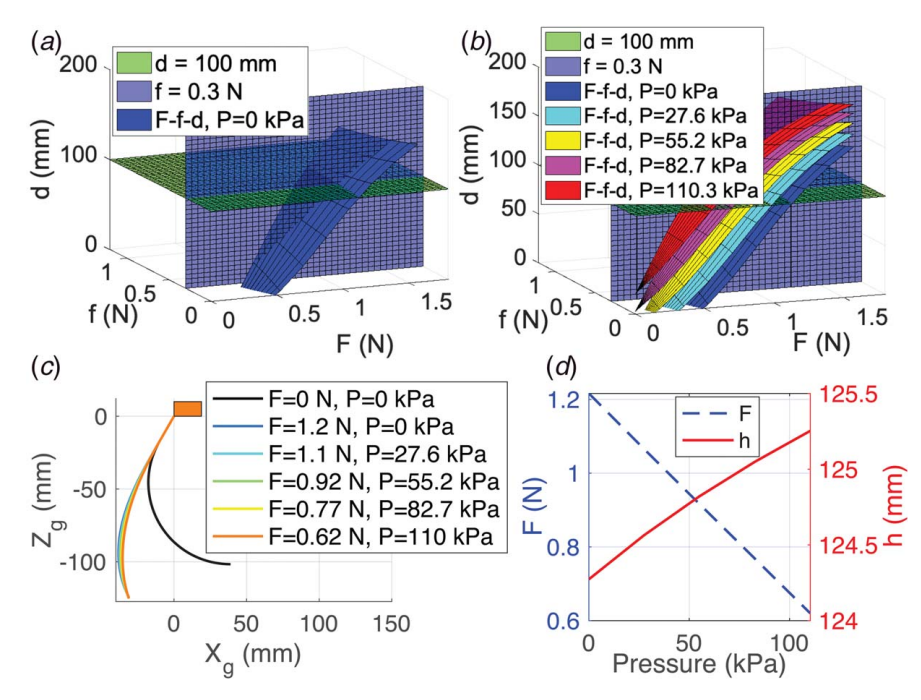


Fig. 10 Contact force control results for a cuboid with d=100 mm and f=0.3 N per finger: (a) intersection of surfaces for zero pressure, (b) intersection of surfaces for different pressures, (c) modeled shapes with different pressures and contact forces F, and (d) contact force and finger height versus pressure

with a pinch grasp at that grasping angle β . Therefore, these cases are dropped out of the grasping region. A dot in Figs. 12(a) and 12(b) implies a valid pinch grasp for that sphere. The dashed lines in Fig. 12(a) indicate that the sphere intersects the finger twice, which contradicts the assumption that there is only one point contact between the finger and the object. Hence, the cases shown as dashed lines are dropped out of the grasping region. Figure 12(c) shows the grasping region, which consists of all the f_v versus r curves for different β , where r is calculated from

$$2r\cos\beta = d\tag{29}$$

Any sphere with a radius and weight per finger in the grasping region can be grasped. The fv_{max} versus r curve represented by the dashed

line shows the largest vertical lifting force each finger can provide for the different sphere radii. It is observed that the gripper is best at grasping intermediate-sized spheres since the curve reaches a maximum value at around r=48 mm. In addition, the larger the positive β (i.e., more enveloping), the heavier the object the gripper can grasp, and the smaller radius and radius range the gripper can grasp. On the other hand, the larger the magnitude of negative β (i.e., more pinching), the lighter the object the gripper can grasp and the larger radius and radius range the gripper can grasp.

5.2.2 Viable Grasping States. For a given sphere, there are multiple robust grasping states which correspond to different grasping angles β . It is desired to know the range of β which results in

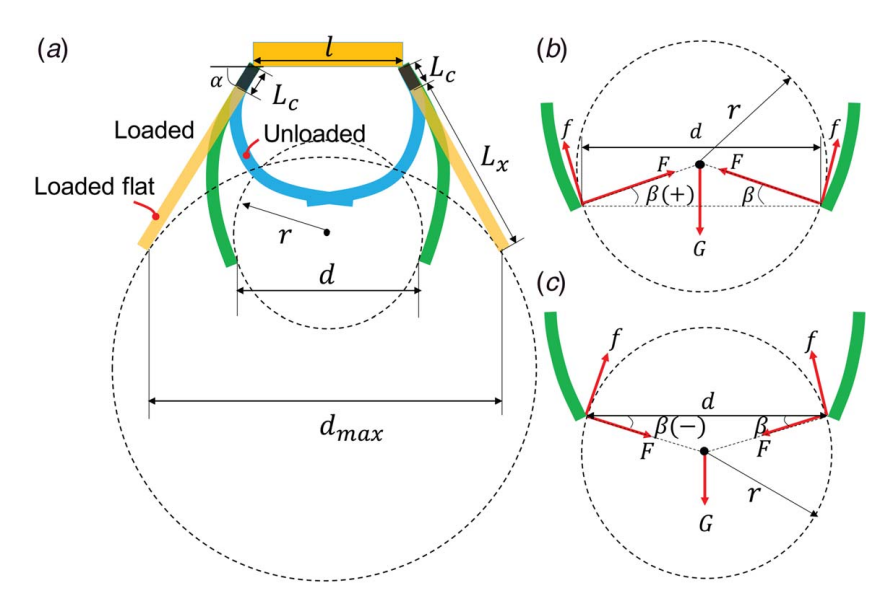


Fig. 11 Gripper grasping spheres: (a) grasping spheres with different sizes, (b) grasping a sphere on its lower half (positive β), and (c) grasping a sphere on its upper half (negative β)

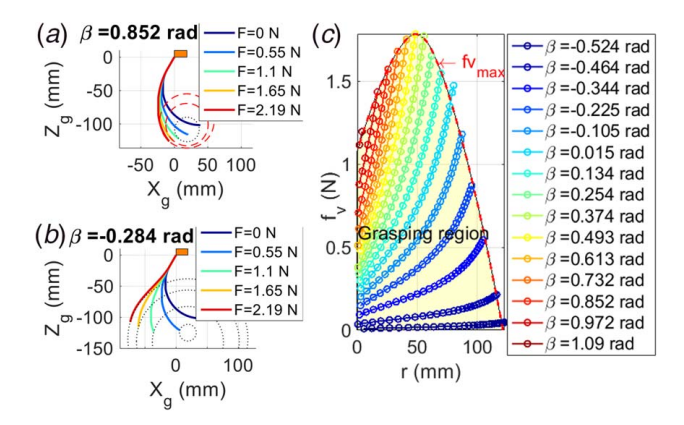


Fig. 12 Gripper grasping capability results for spherical objects: (a) finger shapes for $\beta=0.852$ rad, (b) finger shapes for $\beta=-0.284$ rad, and (c) grasping region, representing the range of object size and weight per finger that can be grasped

robust grasping so that a grasping strategy can be determined before grasping. For illustration purposes, a sphere with radius r = 50 mm and 0.5 N weight per finger is used. In order to determine the grasping states, including forces and shapes applied to the sphere, a three-step approach similar to the method in Sec. 5.1.2 is proposed. Step one: maintain β at a fixed value and run the CCM using different combinations of F and f, where $f \le \mu F$. Then, calculate r using Eq. (29) based on the output d, and plot the surface of $F - f_v - r$, where f_v is calculated from Eq. (27). Step two: find F at the intersection of three surfaces including the $F - f_v - r$ surface and the surfaces for r = 50 mm and $f_v = 0.5$ N. Step three: input F and f to the CCM to find the shape of each finger, where f is calculated from Eq. (27). To find F at different β , $F - f_v - r$ surfaces for different β are generated and the intersections are found using the three steps above, as illustrated in Fig. 13(a). Some of the $F - f_v - r$ surfaces have no intersection point with both surfaces of r = 50 mm and $f_v = 0.5$ N, which means it is impossible to grasp with these β for this sphere. By running the CCM for various β , the range of β for which the $F - f_v - r$ surfaces have single intersection points with both surfaces of r = 50 mm and $f_v = 0.5$ N is found to be [-0.124, 0.4] rad. The modeled shapes of the fingers using upper and lower limits of β are illustrated in Fig. 13(b). A more accurate range of β can be obtained by employing a finer interval of β near the limits, although more computation time is required. With the proposed method, the range of β that results in robust grasping can be determined for a given sphere. Furthermore, this method can be generalized to any object shape with a known geometry, i.e., the grasping angle β which is determined by the gradient of the contact surface and the grasping size at the grasping location.

6 Experiments and Model Validation

Quasi-static measurements of an FPC actuator in response to different pressures and loads are performed with motion capture and loading tests, respectively. FPC actuators are fabricated according to the fabrication process presented in Ref. [18]. A gripper is built with three FPC actuators for demonstration purposes.

6.1 Gripper Demonstration. A soft gripper composed of three FPC actuators, three clamps, and a palm is fabricated as illustrated in Fig. 14, where each actuator is manufactured with 0.4 prestrain. The dimensions and material properties are shown in Tables 3 and 4. All components except the actuators are 3D-printed with PLA using an Ultimaker S5. Applying pressure to the actuators simultaneously allows the gripper to open as it approaches a targeted object. Depressurizing the actuators returns them to their equilibrium precurved shapes, thus closing the gripper and capturing the object. An FPC actuator and a demonstration of the gripper grasping various objects are shown in Fig. 14.

6.2 Motion Capture Tests of Fluidic Prestressed Composite

Actuators. To measure the responses of FPC actuators at different pressures, a quasi-static test has been setup (Fig. 15(a)). A laboratory pneumatic compressed air system is used to pressurize actuators with prestrains of 0.15, 0.25, and 0.4. The pressure is adjusted with a pressure regulator and measured using a pressure gauge. Hemispherical reflective markers with 3 mm diameters are placed along the actuator's mid-plane. A set of four cameras (Opti-Track, Natural Point Inc.) with resolutions of 1.3 megapixels are used to record the position of each marker. The actuator is clamped on a fixture at its root using bolts. The curvature of the actuator is calculated by fitting the positions of the markers to a circle using the least squares method (Fig. 15(b)).

Using the CCM presented in Sec. 3.1 with eight segments of equal length, the shapes of the actuators' mid-planes for three samples with prestrains of 0.15, 0.25, and 0.4 at different pressures are computed using the dimensions and material properties shown in Tables 3 and 4. Figure 16(a) shows the modeled mid-plane shapes for the case with a prestrain of 0.4 at different pressures in the finger's global coordinate frame XOZ. The modeled mid-plane shapes are fit to circles using the method of least squares to compute the curvatures of the actuator. The modeled mid-plane shapes are compared with the corresponding experimentally measured values to validate the CCM (Fig. 16(b)).

In general, the modeled shapes are in agreement with experimental data. It is observed that the higher the prestrain, the smaller the radius of curvature. The discrepancy between the model and data at 0.15 prestrain is due to the stiffening effect of the ribs inside the fluid channel. The ribs behave as thick plates rather than thin plates in the sense of classical laminate theory (thickness $\leq 0.1 \times$ the smallest in-plane dimension). The longitudinal rib is thought

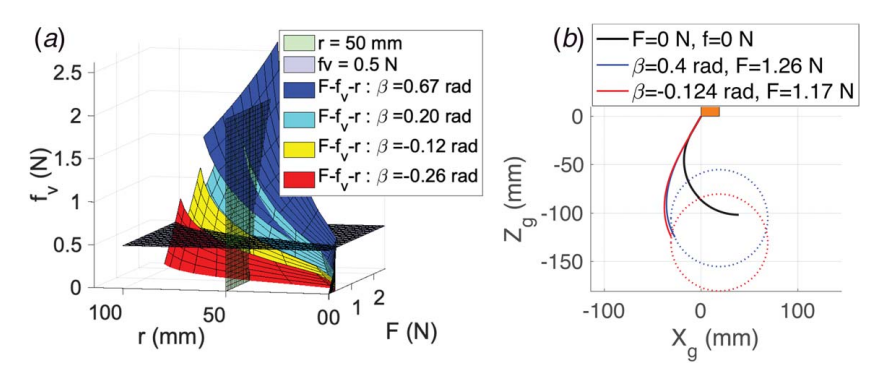


Fig. 13 Grasping states for a sphere with r = 50 mm and $f_v = 0.5$ N per finger: (a) intersections of surfaces for different β and (b) modeled shapes with upper and lower limits of β for robust grasping

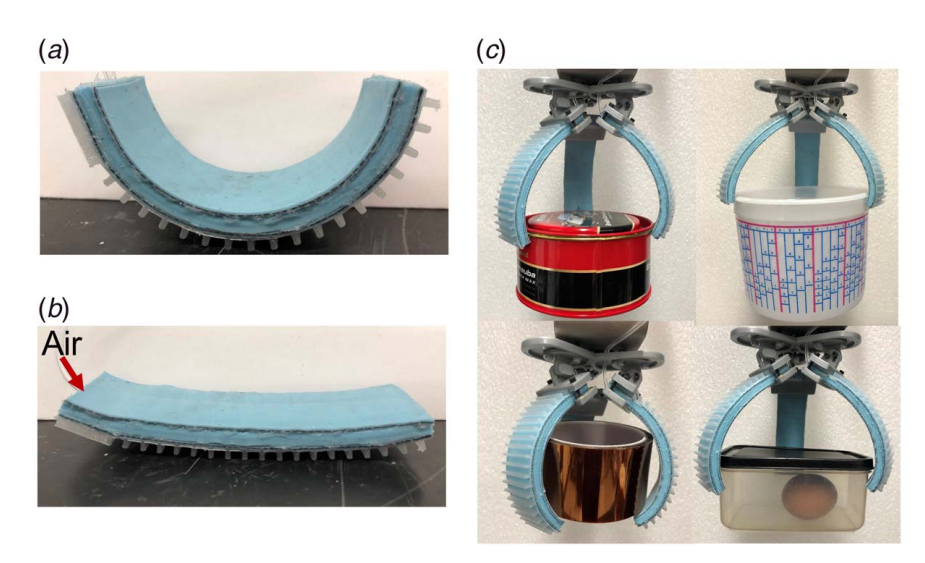


Fig. 14 An FPC actuator with 0.4 prestrain in its (a) unactuated equilibrium precurved shape (0 kPa), (b) actuated almost-flat shape (386 kPa), and (c) demonstration of an FPC gripper grasping different objects

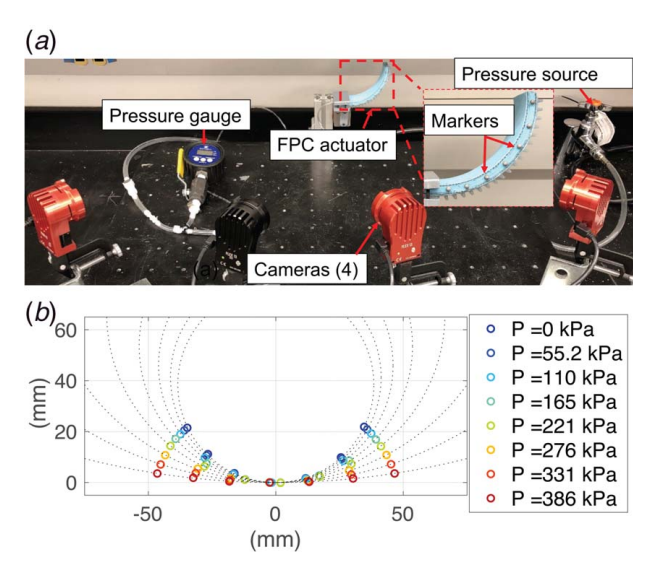
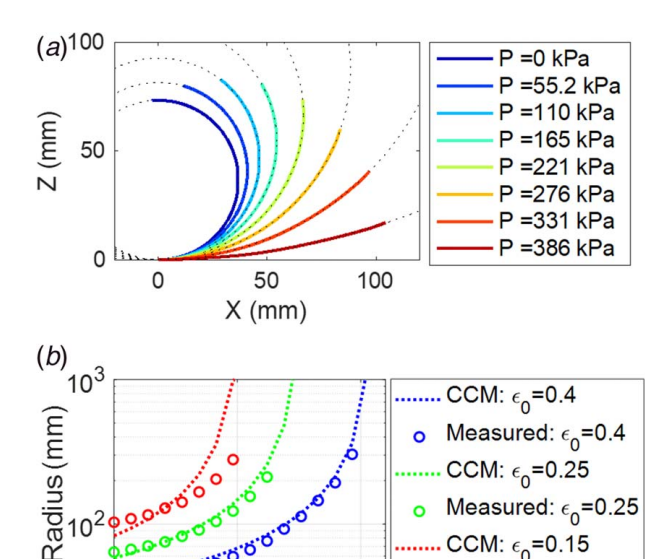


Fig. 15 (a) Motion capture test setup and (b) measured positions of the reflective markers and circular curve fits for an FPC actuator with a prestrain of 0.4 at different pressures

to exacerbate the discrepancy since it is aligned with the direction of curvature. In addition, the ribs in the constraining layer store a small amount of strain energy that our model does not account for. As a result, deforming thick ribs inside the fluid channel and ribs in the constraining layer takes a larger proportion of net energy for 0.15 prestrains than for larger prestrains. Small dimensional variabilities in the fabricated sample may also contribute to the discrepancy. Higher model accuracy can be achieved by including the strain energy of the ribs inside the constraining layer, and incorporating more advanced theories for the analysis of relatively thick plates such as introducing shear deformation plate theory.

6.3 Loading Tests of Fluidic Prestressed Composite Actuators. Loading tests are setup and performed to validate the CCM for both applied end loads and pneumatic pressure (Fig. 17). The same air supply and measurement system as in the motion capture tests are used. The head of the load frame (Mark-10 ES20) moves horizontally and measures the force



Pressure (kPa)

Fig. 16 (a) CCM-modeled shapes of the mid-plane for an FPC actuator with 0.4 prestrain at different pressures and (b) measured and modeled radius of curvature for FPC actuators with different prestrains

0.0.0.0.0.0.0.0

profile with a Mark-10 ME-200 force gauge. A 3D-printed fixture is attached to the actuator's free end and is connected to the force gauge with fishing line. Loading along the X and Z axes in the global coordinate frame of the finger XOZ is demonstrated in Fig. 17. In order to keep the fishing line straight, horizontal, and free of contact with the actuator except for the fixture, the Z-direction test must be performed using a sample with an end slope of less than $\pi/4$, in which case samples with smaller prestrains are required. For the X-direction test, a sample with a higher curvature is preferred as the finger is more bent than drawn along its X direction, which is more common when grasping objects. A sample with a prestrain of 0.4 is tested in the X direction (Fig. 17(α)) and a sample with a prestrain of 0.15 is tested in the X direction (Fig. 17(α)).

Measured: ϵ_0 =0.15

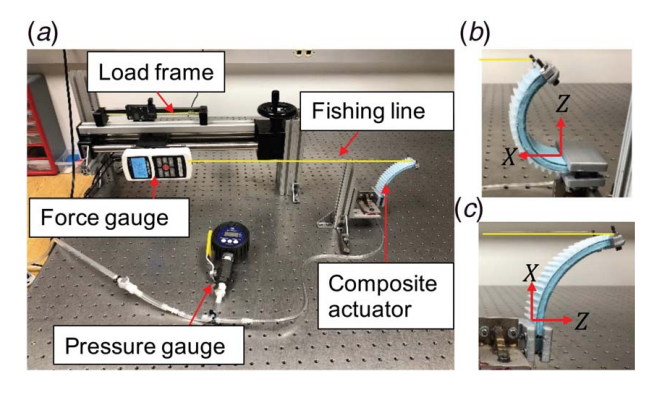


Fig. 17 (a) Loading test setup, (b) loading an actuator (prestrain of 0.4) along the X axis, and (c) loading an actuator (prestrain of 0.15) along the Z axis

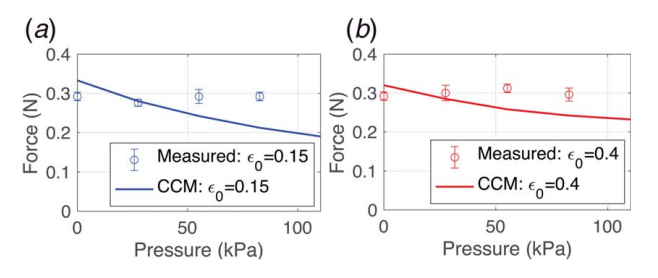


Fig. 18 (a) Force along the X axis versus pressure for the sample with a prestrain of 0.4 at a fixed displacement of 10 mm and (b) force along the Z axis versus pressure for the sample with a prestrain of 0.15 at a fixed displacement of 10 mm

To determine the load responses of FPC actuators at different pressures, forces are measured at a fixed displacement for a series of selected pressures. A four-step experimental procedure is performed at each pressure. Step one: apply a selected pressure without a load and wait several seconds for the actuator to reach its actuated equilibrium shape. Step two: apply a 10 mm displacement to the FPC actuator toward the force gauge and maintain that position. Step three: adjust the actuator's height to align the fishing line that connects the actuator's endpoint and the force gauge to be horizontal, where a ruler is used to measure the heights of two points on the fishing line to ensure that it is level. Step four: measure the force applied to the actuator free end by the fishing line. The four steps above are repeated for different pressures at an increment of 4 psi (27.6 kPa) from 0 to 82.7 kPa. Each loading direction and pressure condition is tested five times for repeatability. The average measurement value and standard deviation are presented.

The forces calculated from the CCM are compared with the corresponding experimentally measured end load to validate the analytical model (Fig. 18). In general, the experimental forces are slightly higher than the modeled ones. This is because the longitudinal rib inside the fluid channel increases the stiffness at larger pressures and the plane-stress assumption underpredicts the forces. Also, the ribs in the constraining layer store a small amount of strain energy that our model does not account for. One can achieve higher model accuracy by including the small amount of strain energy of the ribs in the constraining layer and using more advanced plate theory for thick plates.

7 Conclusions

This paper has presented a modeling framework to analyze the grasping capabilities of a soft gripper based on fluidic prestressed composite actuators using the chained composite model (CCM). The analytical approach provides a means of predicting gripper

and finger performance with explicit relationships between input pressure, actuator shape, and output force. The effects of gripper parameters that influence grasping size and grasping weight are examined through a parametric study. The grasping capabilities and finger shapes for grasping cuboidal and spherical objects are determined through a model-based study. Gentle grasping can be achieved with pressure regulation through model-based force control. The modeling work is also evaluated through experimental characterizations with motion capture and loading tests. The modeled shapes and displacements agree fairly well with the measured responses.

The contributions of this work are summarized as follows. First, the modeling framework presented provides a viable method for designing soft grippers with desired grasping performance. One can extend this modeling framework to grippers based on various types of actuators and obtain their grasping performance by replacing the CCM in our gripper modeling framework with other soft actuator models such as the model for fiber reinforced actuators [25]. Second, the gripper modeling analysis can predict grasping force based on finger and gripper parameters, and external actuation. Third, the proposed modeling framework can be used for controlling grasping force to achieve gentle grasping while maintaining the grasping geometry. In addition, following a similar procedure, grasping of objects with more complex shapes can be analyzed and force control for other shapes can be developed. Future work includes incorporating more advanced theories for the analysis of relatively thick plates to increase model accuracy, investigating more general grasping conditions such as unsymmetrical grasping, developing methods to increase the force capacity such as applying a vacuum, and generalizing the modeling framework to apply it to soft grippers consisting of different kinds of actuators.

Acknowledgment

This research was supported by National Science Foundation, National Robotics Initiative Grant No: CMMI-1637656, and the member organizations of the Smart Vehicle Concepts Center, a Phase III National Science Foundation Industry-University Cooperative Research Center² under Grant NSF IIP 1738723.

Conflict of Interest

There are no conflicts of interest.

Data Availability Statement

The authors attest that all data for this study are included in the paper. Data provided by a third party are listed in Acknowledgment.

References

- Shintake, J., Cacucciolo, V., Floreano, D., and Shea, H., 2018, "Soft Robotic Grippers," Adv. Mater., 30(29), p. 1707035.
- [2] Zou, J., Lin, Y., Ji, C., and Yang, H., 2018, "A Reconfigurable Omnidirectional Soft Robot Based on Caterpillar Locomotion," Soft Rob., 5(2), pp. 164–174.
- [3] Zhou, J., Chen, X., Chang, U., Lu, J.-T., Leung, C. C. Y., Chen, Y., Hu, Y., and Wang, Z., 2019, "A Soft-Robotic Approach to Anthropomorphic Robotic Hand Dexterity," IEEE Access, 7, p. 101483.
- [4] Krahn, J. M., Fabbro, F., and Menon, C., 2017, "A Soft-Touch Gripper for Grasping Delicate Objects," IEEE/ASME Trans. Mechatron., 22(3), pp. 1276– 1286.
- [5] Glick, P., Suresh, S. A., Ruffatto, D., Cutkosky, M., Tolley, M. T., and Parness, A., 2018, "A Soft Robotic Gripper With Gecko-Inspired Adhesive," IEEE Rob. Autom. Lett., 3(2), pp. 903–910.
- [6] Gao, Y., Huang, X., Mann, I. S., and Su, H.-J., 2020, "A Novel Variable Stiffness Compliant Robotic Gripper Based on Layer Jamming," J. Mech. Rob., 12(5), p. 051013.

²http://www.SmartVehicleCenter.org

- [7] Kim, T., Yoon, S. J., and Park, Y.-L., 2018, "Soft Inflatable Sensing Modules for Safe and Interactive Robots," IEEE Rob. Autom. Lett., 3(4), pp. 3216–3223.
- [8] Zhou, Y., Headings, L. M., and Dapino, M. J., 2020, "Discrete Layer Jamming for Variable Stiffness Co-Robot Arms," J. Mech. Rob., 12(1), p. 015001.
- [9] Zeng, X., Hurd, C., Su, H.-J., Song, S., and Wang, J., 2020, "A Parallel-Guided Compliant Mechanism With Variable Stiffness Based on Layer Jamming," Mech. Mach. Theory., 148, p. 103791.
- [10] Polygerinos, P., Correll, N., Morin, S. A., Mosadegh, B., Onal, C. D., Petersen, K., Cianchetti, M., Tolley, M. T., and Shepherd, R. F., 2017, "Soft Robotics: Review of Fluid-Driven Intrinsically Soft Devices; Manufacturing, Sensing, Control, and Applications in Human-Robot Interaction," Adv. Eng. Mater., 19(12), p. 1700016.
- [11] Gorissen, B., Reynaerts, D., Konishi, S., Yoshida, K., Kim, J.-W., and De Volder, M., 2017, "Elastic Inflatable Actuators for Soft Robotic Applications," Adv. Mater., 29(43), p. 1604977.
- Mater., 29(43), p. 1604977.
 [12] Sun, Y., Song, Y. S., and Paik, J., 2013, "Characterization of Silicone Rubber Based Soft Pneumatic Actuators," 2013 IEEE/RSJ International Conference on Intelligent Robots and Systems, Tokyo, Japan, IEEE, pp. 4446–4453.
- [13] Ilievski, F., Mazzeo, A. D., Shepherd, R. F., Chen, X., and Whitesides, G. M., 2011, "Soft Robotics for Chemists," Angew. Chem., Int. Ed., 50(8), pp. 1890– 1805
- [14] Tondu, B., and Lopez, P., 2000, "Modeling and Control of McKibben Artificial Muscle Robot Actuators," IEEE Control Syst. Mag., 20(2), pp. 15–38.
- [15] Hao, Y., Wang, T., Ren, Z., Gong, Z., Wang, H., Yang, X., Guan, S., and Wen, L., 2017, "Modeling and Experiments of a Soft Robotic Gripper in Amphibious Environments," Int. J. Adv. Rob. Syst., 14(3), p. 1729881417707148.

- [16] Wang, Z., and Hirai, S., 2017, "Soft Gripper Dynamics Using a Line-Segment Model With An Optimization-Based Parameter Identification Method," IEEE Rob. Autom. Lett., 2(2), pp. 624–631.
- [17] Li, Y., Chen, Y., Yang, Y., and Wei, Y., 2017, "Passive Particle Jamming and Its Stiffening of Soft Robotic Grippers," IEEE Trans. Rob., 33(2), pp. 446–455.
- [18] Zhou, Y., Headings, L. M., and Dapino, M. J., 2021, "Modeling of Fluidic Prestressed Composite Actuators with Application to Soft Robotic Grippers," IEEE Trans. Rob.
- [19] Zhou, X., Majidi, C., and O'Reilly, O. M., 2015, "Soft Hands: An Analysis of Some Gripping Mechanisms in Soft Robot Design," Int. J. Solids. Struct., 64, pp. 155–165.
- [20] Haibin, Y., Cheng, K., Junfeng, L., and Guilin, Y., 2018, "Modeling of Grasping Force for a Soft Robotic Gripper With Variable Stiffness," Mech. Mach. Theory., 128, pp. 254–274.
- [21] Li, Y., Chen, Y., Ren, T., Li, Y., and Choi, S. H., 2018, "Precharged Pneumatic Soft Actuators and Their Applications to Untethered Soft Robots," Soft Rob., 5(5), pp. 567–575.
- [22] Chillara, V. S., Headings, L. M., and Dapino, M. J., 2016, "Multifunctional Composites With Intrinsic Pressure Actuation and Prestress for Morphing Structures," Composite Struct., 157, pp. 265–274.
- [23] Hyer, M. W., and White, S. R., 2009, Stress Analysis of Fiber-Reinforced Composite Materials, DEStech Publications, Inc, Lancaster, PA.
- [24] Reddy, J. N., 2006, Theory and Analysis of Elastic Plates and Shells, CRC Press, Boca Raton, FL.
- [25] Polygerinos, P., Wang, Z., Overvelde, J. T., Galloway, K. C., Wood, R. J., Bertoldi, K., and Walsh, C. J., 2015, "Modeling of Soft Fiber-Reinforced Bending Actuators," IEEE Trans. Rob., 31(3), pp. 778–789.